Biomaterials 170 (2018) 70–81

Contents lists available at ScienceDirect

Biomaterials

journal homepage: www.elsevier.com/locate/biomaterials

pH protective Y_1 receptor ligand functionalized antiphagocytosis BPLP-WPU micelles for enhanced tumor imaging and therapy with prolonged survival time

Zhenqi Jiang [a, f, 1], Yuchen Tian [a, 1], Dingying Shan [b], Yinjie Wang [a, f], Ethan Gerhard [b], Jianbi Xia [c], Rong Huang [c], Yan He [d], Aiguo Li [d], Jianchao Tang [e], Huimin Ruan [a, f], Yong Li [a], Juan Li [a, **], Jian Yang [b], Aiguo Wu [a, *]

[a] CAS Key Laboratory of Magnetic Materials and Devices, Key Laboratory of Additive Manufacturing Materials of Zhejiang Province, Division of Functional Materials and Nanodevices, Ningbo Institute of Materials Technology and Engineering, Chinese Academy of Sciences, Ningbo 315201, China
[b] Department of Biomedical Engineering, Materials Research Institute, The Huck Institutes of the Life Sciences, The Pennsylvania State University, University Park, PA 16802, USA
[c] Department of Radiology, Department of Pathology, Ningbo No.2 Hospital, Ningbo 315010, China
[d] Shanghai Synchrotron Radiation Facility, Shanghai Institute of Applied Physics, Chinese Academy of Sciences, Shanghai 201204, China
[e] National Centre for Protein Science-Shanghai, Institute of Biochemistry and Cell Biology, Shanghai Institutes for Biological Sciences, Chinese Academy of Sciences, Shanghai 201210, China
[f] University of Chinese Academy of Sciences, Beijing 100049, China

ARTICLE INFO

Article history:
Received 13 February 2018
Received in revised form
28 March 2018
Accepted 1 April 2018
Available online 4 April 2018

Keywords:
pH responsiveness
Antiphagocytosis
BPLP-WPU
Y_1 receptor ligand
Tumor imaging and therapy

ABSTRACT

Nanoparticle-based tumor therapies are extensively studied; however, few are capable of improving patient survival time due to premature drug leakage, off target effects, and poor tissue penetration. Previously, we successfully synthesized a novel family of Y_1 receptor (Y_1R) ligand modified, photoluminescent BPLP nanobubbles and nanoparticles for targeted breast cancer ultrasound imaging; however, increased accumulation could also be observed in the liver, kidney, and spleen, suggesting significant interaction of the particles with macrophages *in vivo*. Herein, for the first time, we imparted antiphagocytosis capability to Y_1R ligand functionalized BPLP-WPU polymeric micelles through the incorporation of a CD47 human glycoprotein based self-peptide. Application of self-peptide modified, DOX loaded micelles *in vivo* resulted in a 100% survival rate and complete tumor necrosis over 100 days of treatment. *In vivo* imaging of SPION loaded, self-peptide modified micelles revealed effective targeting to the tumor site while analysis of iron content demonstrated reduced particle accumulation in the liver and kidney, demonstrating reduced macrophage interaction, as well as a 2-fold increase of particles in the tumor. As these results demonstrate, Y_1R ligand, self-peptide modified BPLP-WPU micelles are capable of target specific cancer treatment and imaging, making them ideal candidates to improve survival rate and tumor reduction clinically.

1. Introduction

Over 250,000 breast cancer diagnoses and over 40,000 breast cancer related deaths were reported in the United States in 2017, contributing to the over 1 million diagnoses and 500,000 deaths worldwide [1,2]. Breast cancer remains the most common cancer afflicting women, necessitating improved clinical treatments [1,2]. Traditional chemotherapeutics rely on the systemic administration of drugs such as doxorubicin (DOX) and imaging agents including super-paramagnetic iron oxide nanoparticle (SPION); however, free drugs and imaging agents suffer from short half-lives *in vivo* as well as significant off-target effects resulting in systemic rather than tumor specific toxicity [3–6]. Thus, non-cytotoxic dosages typically fall well below what is required for effective treatment [5]. In order to improve treatment efficacy, carriers capable of: i) prolonging the half-life of drugs and imaging agents *in vivo*, ii) targeting

* Corresponding author.
** Corresponding author.
E-mail addresses: lij@nimte.ac.cn (J. Li), aiguo@nimte.ac.cn (A. Wu).
[1] These authors contributed equally to this work.

https://doi.org/10.1016/j.biomaterials.2018.04.002
0142-9612/

specifically to tumor cells, and iii) preferentially releasing drugs within the tumor microenvironment are greatly desired.

Nanoparticles have been widely applied for tumor treatment and imaging due to the well-known enhanced permeability and retention (EPR) effect [7,8]. Particularly, polymer coated and polymeric nanoparticles (i.e. poly(lactic acid) (PLA), poly(lactic-co-glycolic acid) (PLGA), poly(ethylene glycol) (PEG), dextran) have risen to prominence as a result of their tailorable surface chemistry, drug encapsulation capability, improved immunogenicity, and biodegradability [9–11]. Such polymeric carriers have been shown to improve the lifetime of drugs and imaging agents in the bloodstream *in vivo*; however, few have demonstrated significant improvement in patient survival times clinically due to suboptimal properties including premature drug leakage during preparation, storage, or blood circulation, lack of active targeting to tumor cells, and poor tissue penetration [12,13]. Recently, citrate-based, intrinsically fluorescent biodegradable photoluminescent polymers (BPLPs) have been developed through a one-pot polycondensation reaction of citric acid, diol, and amino acid. The resulting polymers were further used as macro-initiators for the ring opening polymerization of lactide and glycolide to generate biodegradable and biocompatible, highly photostable BPLP-PLA and BPLP-PLGA nanoparticles [14,15]. The obtained particles were capable of drug encapsulation and sustained drug release, fluorescent cell labelling through particle uptake *in vitro*, and fluorescent tracking *in vivo*, making them ideal candidates for tumor therapy and imaging; however, BPLP based nanoparticles remain non-specific agents with limited imaging depth, diminishing their effectiveness.

Neuropeptide Y Y_1 receptor (Y_1R) is highly over-expressed in many cancers [16,17], which makes it a promising target site for cancer diagnosis and therapy [18–21] capable of reducing off-target effects [5]. In our previous work, a selective Y_1R ligand [Pro^{30}, Nle^{31}, Bpa^{32}, Leu^{34}]NPY(28–36) has been conjugated with nanobubbles or nanoparticles for targeted breast cancer ultrasound imaging and chemotherapy [22,23]. The resulting materials exhibited high affinity for Y_1R overexpressing cells and tumor tissues; however, an increased accumulation of Y_1R ligand-modified nanoparticles in the liver, kidney, and spleen could also be observed, evidence of phagocytosis by macrophages *in vivo* and subsequent localization of the carriers to these macrophage rich and foreign matter clearing organs, as is commonly observed with exogeneous nanoparticles [23–30]. Therefore, it is necessary to develop a novel Y_1R ligand-based nanoparticle delivery system with high specificity to tumors and minimized opsonization to macrophages. To reduce the uptake by macrophages, a self-peptide (SP) designed from human CD47 glycoprotein has been used to impede phagocytosis of nanoparticles by signaling through the phagocyte receptor CD172a, promoting persistent circulation that enhances drug delivery to tumors [31–33]. However, it remains largely unknown whether the Y_1R ligand could synergize with SP for tumor targeting and antiphagocytosis.

The tumor microenvironment, with the characteristics of hypoxia, acidosis, and high interstitial fluid pressure, plays a critical role in tumor proliferation, invasion, and metastasis [34–37]. A prominent feature of the tumor microenvironment, acidosis arises from over-production of lactic acid and carbon dioxide by tumor cells as well as the hypoxic environment of the core of solid tumors [38]. A number of pH-sensitive nanoparticles have been developed to respond to the acidic tumor microenvironment, thus improving their stability during storage and blood circulation, limiting off-target drug release and concomitantly enhancing drug release and thus effectiveness in the tumor microenvironment [5,39–42]. To further improve the targeting of nanoparticles to tumor cells, active targeting ligands or peptides have been connected to pH responsive materials to form environment sensitive nanoparticles [43–46]. For example, cell penetrating peptide $(R_2)_2$ was connected to pH trigger sequence H_7 to form tumor-specific pH-responsive peptide $H_7K(R_2)_2$, for targeted anti-glioma therapy [47]. Nonetheless, there are few intrinsic peptides with both pH-response and active targeting properties.

In this work, novel biodegradable photoluminescent water-borne polyurethane polymers (BPLP-WPU) were synthesized for the preparation of Y_1R ligand [Asn^6, Pro^{34}]-NPY (AP) [48] and SP co-modified SPION or DOX loaded BPLP-WPU micelles (BWM). Tumor targeting, antiphagocytosis, magnetic resonance imaging (MRI) performance, and therapeutic effects of the prepared SPION or DOX-loaded AP&SP-BWM were evaluated *in vitro* and *in vivo*. Results demonstrated that: i) encapsulation of DOX within and modification of BPLP-WPU with acid sensitive AP and SP is capable of prolonging particle lifetime in the bloodstream, reducing particle phagocytosis, and minimizing off-target drug release, ii) Y_1R ligand enables specific targeting of nanoparticles to Y_1R overexpressing tumor cells, enhancing drug accumulation and local concentration, and iii) addition of the acid responsive AP moiety may reduce systemic drug release while enhancing local release in tumors.

Furthermore, the combination of AP and SP enhanced the T_2-MR signal of AP&SP-BWM-SPION in tumors, as well as the therapeutic effects of AP&SP-BWM-DOX in MCF-7 tumor bearing mice, resulting in prolonged survival time. AP&SP-BWM-SPION/DOX is established as a novel, biocompatible, biodegradable nanocarrier with enhanced lifetime, targeting specificity, and environmentally responsive drug release combined with both fluorescent and MRI imaging capabilities, demonstrating great promise as a clinically relevant chemotherapeutic agent (Scheme 1).

2. Materials and methods

2.1. Materials

Ethanol, 1-ethyl-3-(3-dimethylaminopropyl) carbodiimide hydrochloride (EDAC) and *N*-hydroxysuccinimide (NHS), 3-(4,5-dimethylthiazol-2-yl)-2,5 diphenyltetrazolium bromide (MTT), HPLC grade acetonitrile and trifluoroacetic acid (TFA) were purchased from Aladdin Industrial Inc (Shanghai, China). Dulbecco's Modified Eagle Medium (DMEM), RPMI-1640 medium, fetal bovine serum (FBS), penicillin, and streptomycin were purchased from Invitrogen™ (Carlsbad, USA). [Asn^6, Pro^{34}]-NPY (AP) (YPSKPNNP-GEDAPAEDLARYYSALRHYINLITRPRY-NH_2) and self-peptide (SP) (GNYTCEVTELTREGETIIELK-NH_2) were synthesized by the Dechi Biosciences Co, Ltd (Shanghai, China). FITC phalloidin and DOX hydrochloride were purchased from Sigma-Aldrich Co. LLC (Shanghai, China). All reagents were used as received.

2.2. BPLP-WPU polymer synthesis

BPLP synthesis: Biodegradable photoluminescent polymer (BPLP) was prepared through a one-pot polycondensation reaction. First, citric acid (CA), 1, 8-octanediol (OD), and L-serine with the molar ratio of 1:1.1:0.2 were mixed and melted in a round-bottom flask at 160 °C for 20 min. The temperature was reduced to 140 °C, and the reaction progressed for an additional 1.5 h. The prepared BPLP pre-polymer was dissolved in 1, 4-dioxane and purified by precipitating the solution into distilled water. Finally, the purified pre-polymer was freeze-dried and stored at −20 °C for further use.

BPLP-WPU synthesis: In the first step, excess isophorone diisocyanate and polyethylene glycol (PEG) with the molecular weight of 2000 were reacted with stannous (II) octoate (Sn(II) Oct) catalyst in a round-bottom flask at 85 °C for 1 h. BPLP solution in acetone was added to the flask and reacted for another hour under reflux. In the

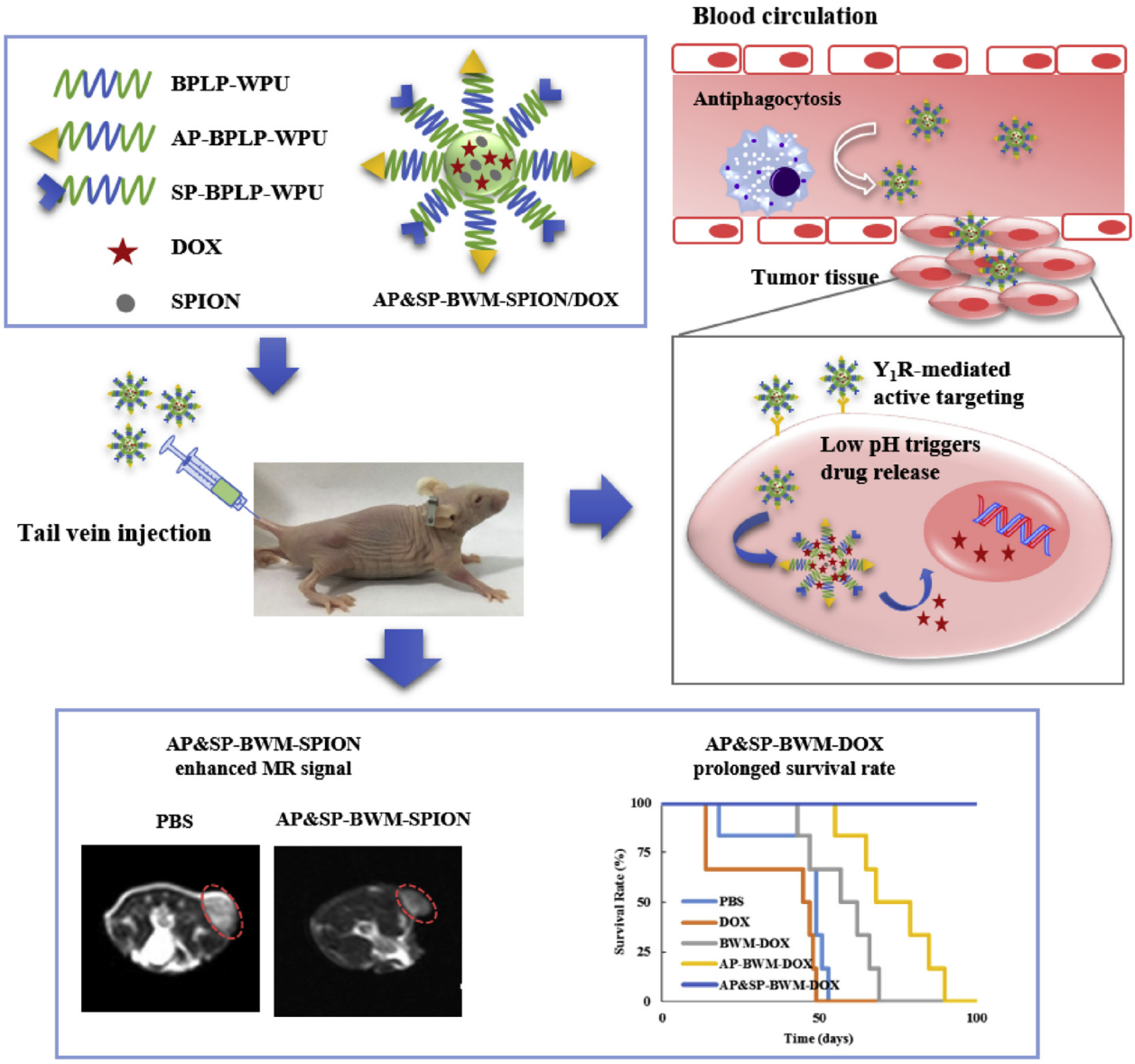

Scheme 1. Y_1 receptor ligand [Asn^6, Pro^{34}]-NPY (AP) and self peptide (SP) functionalized novel BPLP-WPU micelles (BWM) could avoid premature drug leakage and macrophage opsonization during systemic circulation. AP modification further improved micelle targeting to the tumor cells and promoted drug release in the acidic tumor microenvironment. The reduced accumulation in liver and kidney enhanced the specific targeting and high retention of micelles in tumors, generating excellent magnetic resonance signal and therapeutic efficacy with prolonged survival time.

third step, 1, 4-butanediol and 2, 2-bis(hydroxymethyl)propionic acid were incorporated into the macromonomer backbone to prepare BPLP-WPU pre-polymer with carboxylic acid. Carboxylic acid was neutralized with trimethylamine (TEA), and the anionic polyurethane pre-polymer was prepared. Finally, the anionic polyurethane pre-polymer was vigorously sheared and stirred in water with ethylenediamine. After further chain extension in water, the residual isocyanate groups were completely transformed into urea linkages. The obtained fluorescent anionic waterborne polyurethane BPLP-WPU was dispersed in water.

2.3. AP/SP-BPLP-WPU copolymer synthesis and characterization

AP/SP-BPLP-WPU synthesis: AP or SP modified BPLP-WPU copolymer was synthesized by substitution reaction. Briefly, BPLP-WPU, EDAC, and NHS (1:1:1.5 mol ratio) were mixed in water for 4 h at room temperature. The molar equivalent to BPLP-WPU of AP (or SP) was added into activated solution, and the mixture was stirred for 24 h at room temperature. The resulting product was purified by dialyzing against water (MWCO: 15 KDa) over night and then lyophilized. The resulting copolymer was AP-BPLP-WPU (or SP-BPLP-WPU).

AP&SP-BWM-DOX/SPION preparation: Blank micelles and doxorubicin·HCl (DOX·HCl) or superparamagnetic iron oxide nanoparticle (SPION) [49] loaded micelles were prepared via a solvent evaporation method [14]. Briefly, 2 mL of ethanol containing 1 mg DOX·HCl (or 2 mg SPION) and 25 mg BPLP-WPU (or BPLP-WPU:AP-BPLP-WPU = 25:1, *w/w*; BPLP-WPU:AP-BPLP-WPU:SP-BPLP-WPU = 100:4:1, *w/w/w*) was injected dropwise into 10 mL of PBS under magnetic stirring for 16 h. The organic solvent was eliminated by evaporation at room temperature. Un-encapsulated free DOX·HCl was removed by ultrafiltration (MWCO: 10 KDa, Millipore Co., USA). The supernatant was BWM-DOX/SPION (or AP-BWM-DOX/SPION, AP&SP-BWM-DOX/SPION). The encapsulated

DOX concentration was tested by UV detection (Lambda 950, Perkin Elmer, USA) at a wavelength of 480 nm, and the encapsulated SPION concentration was tested by ICP-MS (NexION 300, Perkin-Elmer, USA).

Particle size, size distribution, and zeta potential of the nano-micelle dispersions were measured at room temperature by dynamic light scattering (DLS) using a Zeta particle size analyzer (Nano-ZS, Malvern, England). The data was collected on an auto-correlator with a detection angle of 173°. To obtain detailed structural and morphological information, ~1 μL of the diluted micelle dispersion was dropped onto a copper grid coated with a thin layer of carbon film and then dried at room temperature. High-resolution transmission electron microscopy (HRTEM) images were recorded from a JEOL-2100 (JEOL, Japan) instrument, which was operated at 200 kV.

2.4. pH dependent drug release

In vitro pH-sensitive drug release was determined using a dynamic dialysis method [50] conducted at 37 °C. Typically, 1 mL of micelles in PBS (pH 7.4) were placed into a dialysis bag (MWCO: 2 KDa) and dialyzed against 49 mL of PBS (pH 7.4 or 5.0) in an oscillation incubator at 100 rpm. At hourly intervals, a 1 mL sample was removed from the release medium and an equal volume of PBS was replaced. The amount of DOX was determined using a T10CS UV–Vis spectrophotometer (Persee, China) at 480 nm and percent cumulative release was calculated via a previous method [51].

2.5. Cell culture and transfection

Human breast cancer MCF-7 cell line was cultured in Dulbecco's modified Eagle's medium (DMEM). Human leukemia monocytic THP-1 cell line and mouse peritoneal macrophage Raw 264.7 cell line were cultured in RPMI-1640 medium. Medium was supplemented with 10 wt % fetal bovine serum (FBS), 100 units/mL of penicillin, and 100 mg/mL of streptomycin. The cells were maintained in a 37 °C incubator with 5% CO_2. Differentiation of THP-1 cells was achieved in 100 ng/mL phorbol myristate acetate (PMA, Medchem Express, USA) for 2 days and confirmed by cell attachment to tissue-culture plastic [40]. All cells are from the Cell Bank of the Chinese Academy of Sciences (Shanghai, China).

2.6. Cell cytotoxicity assay

MCF-7 cells were seeded in 96-well culture plates at a density of 1×10^4 cells/well, and grown for 24 h. The medium was replaced with free DOX, BWM-DOX, AP-BWM-DOX, or AP&SP-BWM-DOX in the DOX concentration range of 0.3–80 μg/mL for 24 h at 37 °C. 10 μL of MTT solution (5 mg/mL in PBS) was added into each well followed by 4 h incubation at 37 °C in darkness, after which the medium was removed and 200 μL DMSO was added. Measurement was performed using an automated plate reader (iMark (168–1130), Biorad, USA) at 550 nm. Relative cell viability was calculated by comparing the absorbance intensity of groups treated with different drug-loaded micelles with the control group. Cell inhibition rate = 1−cell viability. The drug concentration of inhibition of 50% cell growth (IC_{50}) was calculated by SPSS 18.0.

2.7. Cellular uptake in MCF-7 cells and macrophages

For LSCM analysis, confocal culture dishes (NETS Co., USA) were used. 2.0 mL MCF-7 cells in complete DMEM medium were seeded into each dish at 5×10^4 cells/mL and allowed to adhere for 24 h. The medium was then removed and treated with fresh medium containing free DOX, BWM/DOX, AP-BWM/DOX, or AP&SP-BWM/DOX solution (DOX: 5 μg/mL). After a further 4 h incubation, the cells were washed three times with PBS to remove any adsorbed free micelles. Afterward, the cells were fixed with 4% formaldehyde for 30 min, treated with 0.1% triton for 5 min, and then treated with 1.0% BSA for 30 min and treated with FITC phalloidin (5 μg/mL) for 30 min at room temperature. Finally, the samples were simultaneously excited at 488 nm and the fluorescent images at emission wavelengths of 480–540 and 560–620 nm were observed by a LSCM (TCS SP5 II, Leica, Germany).

For flow cytometry analysis, six-well plates coated with 0.01% poly (Lys) were used. 2.0 mL of MCF-7, THP-1, or RAW 264.7 cells in complete DMEM or RPMI-1640 medium (for THP-1, RPMI-1640 was supplemented with 100 ng/mL PMA) were seeded into each well at 5×10^4 cells/mL and allowed to adhere for 24 h. The medium was then removed and treated with fresh medium containing BWM, AP-BWM, or AP&SP-BWM (100 μg/mL). After a further 8 h incubation, the cells were washed three times with PBS to remove any adsorbed free nanoparticles. Afterward, the cells were detached with trypsin-EDTA and resuspended in a proper volume of PBS for flow cytometer analysis (FACSCalibur, BD, USA). The mean fluorescence intensity (MFI) from 1×10^4 cells were analyzed, where the gate was arbitrarily set for the detection of Indo 1 Violet-A (351–356 nm) with forward and side scattering dot ploys used to discriminate cellular debris.

2.8. In vitro magnetic resonance imaging (MRI) analysis

The *in vitro* relaxation times (T_1 and T_2) of BWM-SPION, AP-BWM-SPION, and AP&SP-BWM-SPION were measured on a 0.47 T Micro MR instrument at the frequency of 23.318 MHz (Niumag, Shanghai, China). Dilutions of BWM-SPION, AP-BWM-SPION, and AP&SP-BWM-SPION samples in Milli-Q water with various Fe concentrations (0, 0.15, 0.3, 0.6, 1.2, and 2.4 mM) were placed in a tube holder for relaxivity measurements (Tw = 3000 ms). Values of T_1 and T_2 were measured, and then longitudinal (r_1) and transverse (r_2) relaxivities were calculated from the slope of inverse relaxation times ($1/T_1$ and $1/T_2$) plotted against different Fe concentrations. The T_2-weighted images of different samples with various Fe concentrations were acquired on a 0.47 T Micro MR instrument (TR = 2000 ms, TE = 60 ms).

2.9. Tumor model

All experimental protocols involving animals were approved by the Regional Ethics Committee for Animal Experiments at Ningbo University (Permit No. SYXK Zhe 2013-0191). Female Balb/c nude mice (18–20 g, 4–6 weeks old) were purchased from Bikai Biological products sales center (Nanjing, China). The human breast cancer tumor model was established by subcutaneous injection of MCF-7 cells. Briefly, MCF-7 cells (1×10^7 cells for one mouse) suspended in 100 μL of serum free medium were inoculated subcutaneously in the back of nude mice. A digital caliper was used to measure the tumor size. Tumor volume = (tumor length) × (tumor width)^2/2.

2.10. In vivo MRI and biodistribution of Fe

For *in vivo* MRI, nine MCF-7 tumor bearing nude mice were divided into three groups and first anesthetized by intraperitoneal injection of chloral hydrate solution (5 wt %), and then 100 μL of the BWM-SPION, AP-BWM-SPION or AP&SP-BWM-SPION (15 mg/kg for Fe) aqueous solution was administrated intravenously. The T_2-weighted images were acquired using a 1.5 T human clinical scanner (Ingenia 1.5 T, Philips, the Netherlands).

For *in vivo* biodistribution of Fe, MCF-7 tumor bearing nude mice were randomly divided into four groups (3 each group), then 100 μL

PBS, BWM-SPION, AP-BWM-SPION, or AP&SP-BWM-SPION (15 mg/kg for Fe) solution was administrated intravenously into the mice. After 24 h, the mice were sacrificed and the distribution of Fe in main organs including heart, liver, spleen, kidney, lung, and tumor was determined by ICP-MS analysis as previously reported [52]. For ICP-MS analysis, these organs were lyophilized and weighed before digestion in aqua regia for 4 h under heat treatment at 95 °C for tissue dissolution. The concentration of Fe in these organs was then quantified.

2.11. In vivo antitumor activity

MCF-7 tumor bearing nude mice with tumor volumes of 40–60 mm^3 were divided into five groups (6 each group) and treated via tail vein injection of PBS, DOX, BWM-DOX, AP-BWM-DOX, or AP&SP-BWM-DOX (100 μL, 5 mg/kg for DOX). The DOX loaded micelles were intravenously administered to mice on 0, 2, 4, 6, 8, and 10 days. During the treatment process, tumor volume and body weight were measured every day. After treatment, death of mice from each group was recorded for 100 days for calculation of survival rate. The major organs including heart, liver, kidney, lung, and spleen were stained with hematoxylin and eosin (H&E) and examined with a DMI3000 optical microscope (Leica, Germany). Blood was collected by a cardiac puncture method for hematological analysis by a blood analyzer (Sysmex XT-1800i, Japan).

2.12. Pharmacokinetics study

Groups of five Balb/c mice were administered with DOX or AP&SP-BWM-DOX via tail vein (5 mg/kg for DOX). The blood samples (0.5 mL) were collected at the indicated time after injection (1 min, 10 min, 30 min, 1 h, 2 h, 8 h, 12 h and 24 h), and the plasma was separated with centrifugation at 4500 rpm for 10 min. 200 μL plasma were extracted with chloroform/methanol (4:1, *v/v*), and the extractions were then subjected to HPLC assay. An Agilent 1260 infinity liquid chromatography system was used for DOX concentration measurement. The mobile phase was methanol and water solution containing 0.1% formic acid (80:20, *v/v*), and the flow rate was 1.0 mL/min. On the other hand, groups of five Balb/c mice were administered with SPOION or AP&SP-BWM-SPION via tail vein (15 mg/kg for Fe). At the indicated time after injection (1 min, 10 min, 30 min, 1 h, 2 h, 8 h, 12 h and 24 h), the blood sample (0.5 mL) was collected and digested with aqua regia at 95 °C, and then quantified via inductively coupled plasma optical emission spectrometry (ICP-OES). Pharmacokinetic parameters were calculated by two-compartmental data analysis of blood concentrations.

3. Results and discussion

3.1. Synthesis and characterization of AP&SP-BWM-SPION/DOX

BPLP-WPU polymers with unique intrinsic fluorescence were first synthesized and the chemical structures were confirmed with ATR-FTIR and NMR (Fig. S1). In the ATR-FTIR spectrum (Fig. S1c), the absorption peaks at 1697 cm^{-1} (-C(=O)OR), 2908 cm^{-1} (−CH_2−), 3322 cm^{-1} (N−H), 1536 cm^{-1} (C−N−H), and 1456 cm^{-1} (−CH_2−) were assigned to the ester group of BPLP, methylene group from 1,8-octanediol and 1,4-butanediol, urethane in the hydrogen bond, urethane group, and methylene group from PEG, respectively. In the ^{1}H NMR spectrum of BPLP-WPU (Fig. S1d), the peaks at 0.95 ppm, 1.66 ppm, 2.75 ppm, 3.27 ppm, and 3.51 ppm were assigned to the −CH_3 from isophorone diisocyanate, −CH_2− from 1,8-octanediol and 1,4-butanediol, −CH_2− from citric acid, −CH_2− from TEA, and −CH_2− from PEG, respectively. Both ATR-FTIR and ^{1}H NMR results confirmed the successful synthesis of BPLP-WPU.

AP&SP-BWM-SPION/DOX micelles were further prepared

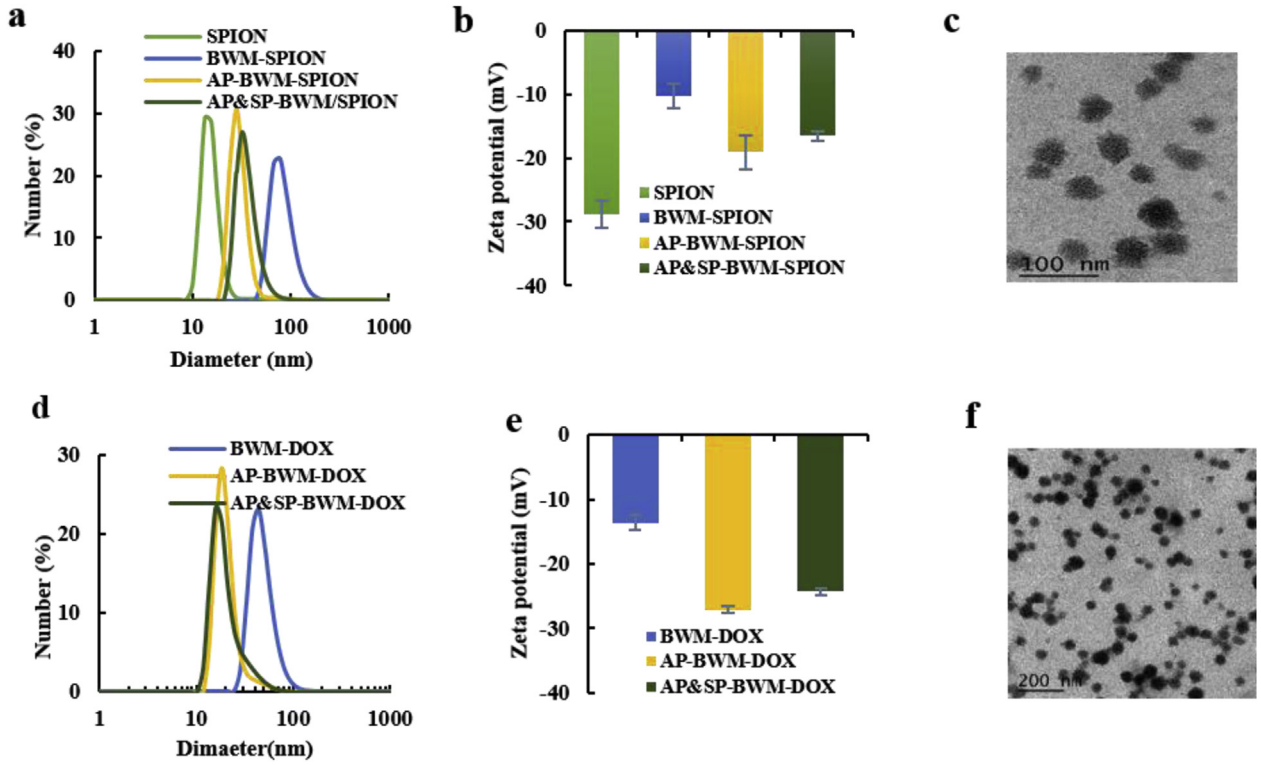

Fig. 1. Characterization of AP&SP-BWM-SPION/DOX. a, b, c) DLS, zeta potential and TEM images of SPION, BWM-SPION, AP-BWM-SPION, and AP&SP-BWM-SPION. d, e, f) DLS, Zeta potential and TEM image of BWM-DOX, AP-BWM-DOX, and AP&SP-BWM-DOX.

through a solvent evaporation method [14], and characterized by dynamic light scattering (DLS) and transmission electron microscopy (TEM) (Fig. 1). The mean diameters of BWM-SPION, AP-BWM-SPION, and AP&SP-BWM-SPION were 68.2 ± 3.1 nm, 31.1 ± 2.0 nm, and 33.5 ± 2.2 nm (PDI<0.223), with negative zeta potentials of −10.3 ± 1.9 mV, −19.1 ± 2.7 mV, and −16.5 ± 0.8 mV in

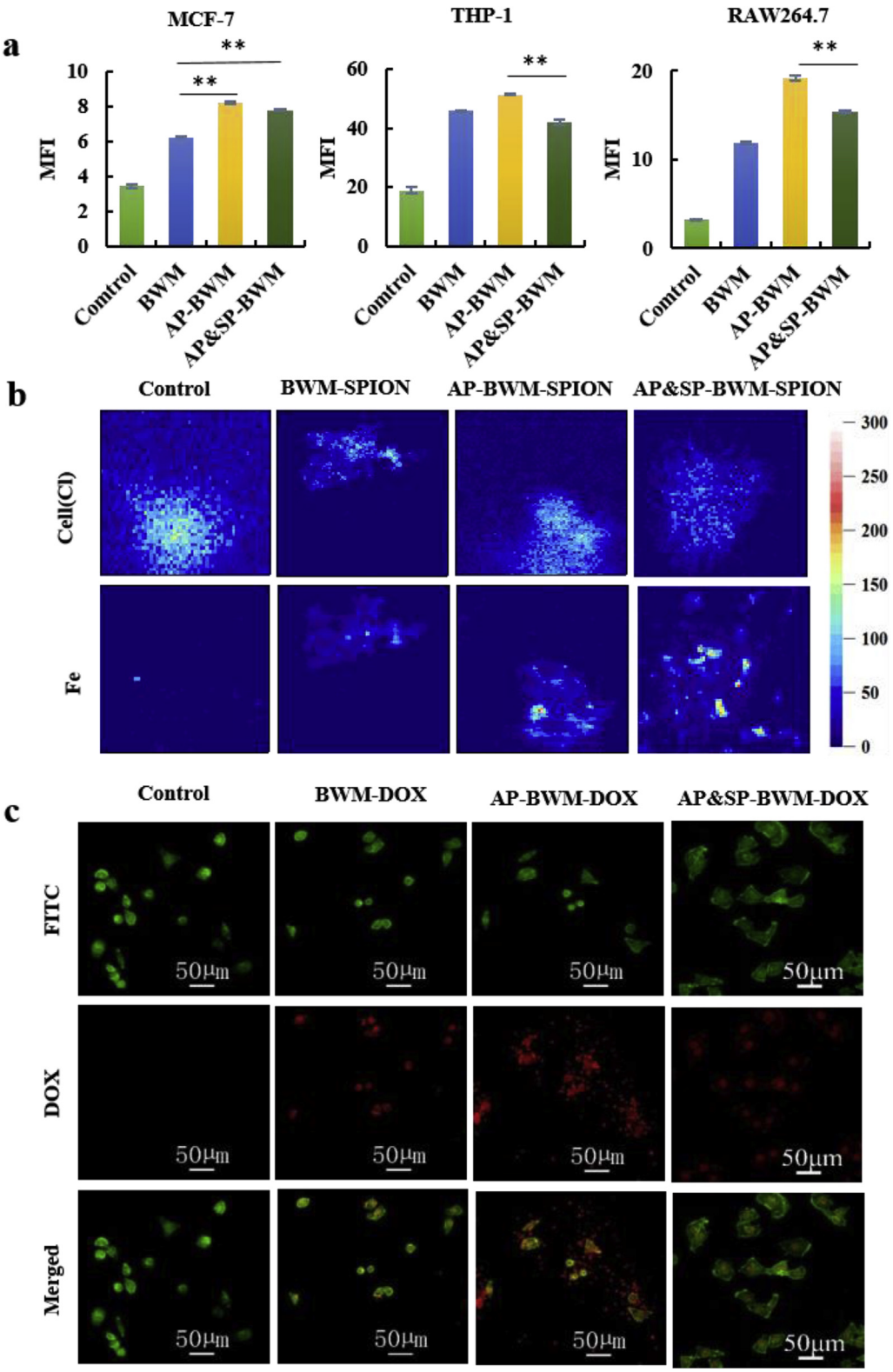

Fig. 2. Cellular uptake of AP&SP-BWM-SPION/DOX. a) Mean fluorescence intensity (MFI) of MCF-7, THP-1, and RAW264.7 cells incubated with BWM, AP-BWM, and AP&SP-BWM for 8 h, followed by flow cytometry analysis (EX 335 nm, EM 351–356 nm). Mean ± SD ($n = 3$), $^{**}P < 0.01$. (BPLP-WPU = 100 μg/mL) b) X-ray fluorescence images (XFM) of MCF-7 cells treated with BWM-SPION, AP-BWM-SPION, or AP&SP-BWM-SPION for 8 h. Fe concentration is 0.2 mM c) Confocal microscopy images of MCF-7 cells incubated with BWM-DOX, AP-BWM-DOX, or AP&SP-BWM-DOX for 8 h. DOX concentration is 5 μg/mL.

PBS, respectively (Fig. 1a and b and Table S1). TEM images showed that AP&SP-BWM-SPION was uniform in size (Fig. 1c). On the other hand, the mean diameter of BWM-DOX, AP-BWM-DOX, and AP&SP-BWM-DOX were 43.5 ± 2.3 nm, 21.4 ± 1.2 nm, and 23.8 ± 1.3 nm (PDI < 0.276), with negative zeta potentials of -13.6 ± 1.1 mV, -27.1 ± 0.6 mV, and -24.3 ± 0.5 mV in PBS, respectively (Fig. 1d and e and Table S2). These results indicate that modification of micelles with AP and SP leads to a more anionic surface character along with a reduction of micelle size, with no significant difference observed between AP and AP&SP modified micelles. Additionally, the diameter of AP&SP-BWM-DOX showed no obvious change after 60 days at 4 °C in PBS (pH = 7.4) (Fig. S2). Further, the size change of AP&SP-BWM-SPION and AP&SP-BWM-DOX has also been tested in a simulated blood environment (Fig. S3). There was only a slight size change could be found for both micelles in PBS with 10% FBS (pH = 7.4) at 37 °C for 72 h under the oscillation, suggesting good stability for both micelles.

3.2. *In vitro targeting and antiphagocytosis effect of AP&SP-BWM-SPION/DOX*

In vitro targeting of AP&SP-BWM was assessed using human breast cancer MCF-7 cell line, known to highly overexpress Y_1R [23]. Due to the photoluminescent property of the prepared micelles, flow cytometry analysis was used to quantify the cellular uptake of micelles (EX 335 nm, EM 351–356 nm). Fig. 2a showed that AP-BWM (8.23) and AP&SP-BWM (7.81) treated MCF-7 cells had much higher mean fluorescence intensity (MFI) than BWM (6.25). This result suggested that the modification of AP and SP improved the delivery of BWM into the MCF-7 cells. Further, *in vitro* antiphagocytosis of AP&SP-BWM was investigated with human leukemia monocytic THP-1 cell line and mouse peritoneal macrophage Raw 264.7 cell line. THP-1 cells were differentiated in RPMI-1640 medium supplemented with 100 ng/mL phorbol myristate acetate (PMA) for 48 h. The effect of different proportions of SP-BPLP-WPU in AP&SP-BWM on the cellular uptake of THP-1 and RAW 264.7 cells was investigated (Fig. S4). It was found that the proportion of 100:1 (BPLP-WPU:SP-BPLP-WPU, *w/w*) generated the lowest MFI for both THP-1 and RAW 264.7 cells, suggesting a reduced uptake of AP&SP-BWM in both cells at this proportion. Fig. 2a indicated that the MFI of THP-1 and RAW 264.7 cells treated with AP&SP-BWM were much lower than that of AP-BWM, which were 42.03 and 51.36 for THP-1 cells, and 15.4 and 19.17 for RAW 264.7 cells, respectively, suggesting that the SP modification significantly decreases the delivery of AP-BWM into both human and mouse macrophages; however, uptake of both AP-BWM and AP&SP-BWM by both cell lines was increased compared to BWM alone. As noted above, zeta potentials for modified BWM are lower than unmodified BWM, indicating a more anionic surface character in the modified polymers. Previous research has indicated increased interaction and uptake of anionic nanoparticles with macrophage cells, matching the results obtained in Fig. 2a, where relatively anionic AP-BWM and AP&SP-BWM display increased uptake [53]. Modification with SP effectively decreases uptake versus AP-BWM, indicating the effectiveness of the SP; however, surface charge remains the dominant effector in micelle/macrophage interactions. Conversely, when micelles are exposed to MCF-7 cells, AP-BWM and AP&SP-BWM display increased uptake due to the active targeting effect of Y_1R ligand despite the generally less favorable interactions of anionic particles with tumor cells compared to cationic particles, indicating that specific targeting is the dominant effector compared to surface charge in micelle/tumor cell interactions [53]. These results indicate the beneficial effect of SP modification as well as the effectiveness of the targeting ligand.

To acquire a direct visual and quantitative localization of SPION-loaded AP&SP-BWM in MCF-7 cells, X-ray fluorescence imaging

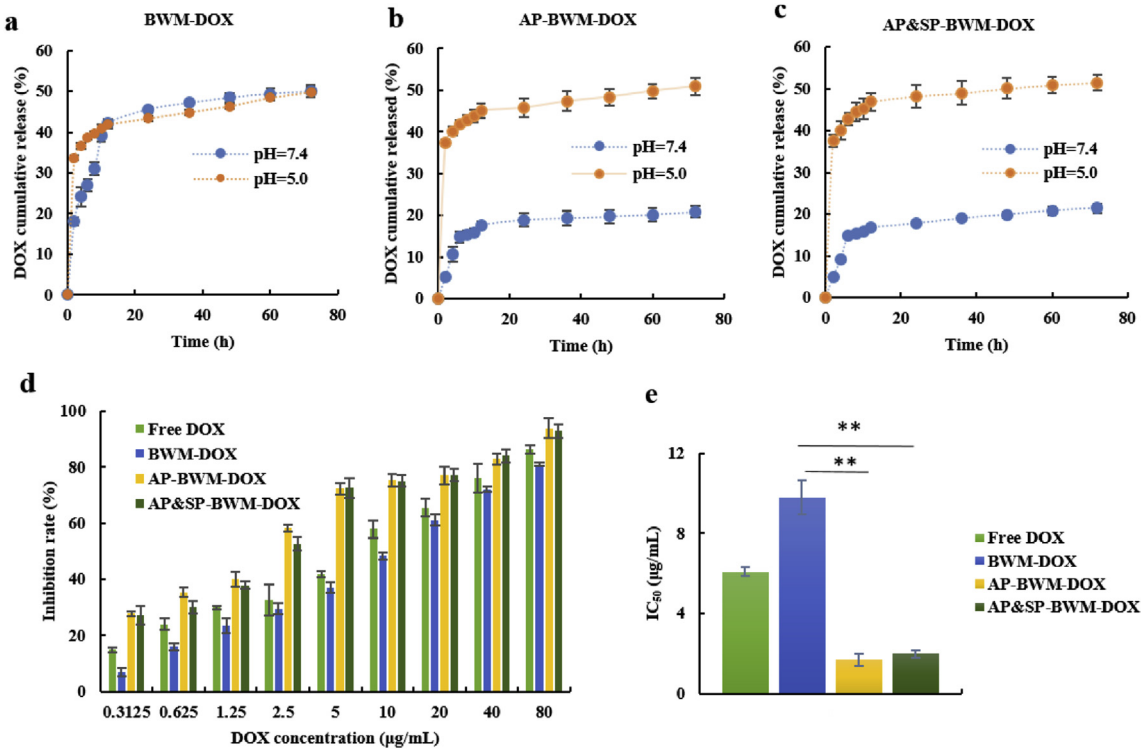

Fig. 3. *In vitro* drug release and cytotoxicity of AP&SP-BWM-DOX. (DOX = 1 mg/mL) a, b, c) *In vitro* cumulative release of DOX from BWM-DOX, AP-BWM-DOX, and AP&SP-BWM-DOX in PBS (pH = 7.4 or 5.0) for 72 h at 37 °C. d) Cell inhibition rate of AP&SP-BWM-DOX at different DOX concentrations. e) IC_{50} value of free DOX, BWM-DOX, AP-BWM-DOX, and AP&SP-BWM-DOX. Mean ± SD (n = 3), $^{**}P < 0.01$.

(XFM) was carried out to map elemental fluorescence of Fe in the cells [54–56]. In Fig. 2b, the biogenic element chlorine was used to map the MCF-7 cells, and Geo 32 color was used to indicate low and high amounts of Fe. The fluorescence intensity of AP-BWM-SPION and AP&SP-BWM-SPION were much higher than BWM-SPION, suggesting that AP modification improves the uptake of BWM-SPION in MCF-7 cells, but the SP modification doesn't reduce this effect.

Additionally, the cellular uptake of DOX-loaded AP&SP-BWM in MCF-7 cells was also investigated by laser scanning confocal microscopy (LSCM). The samples were simultaneously excited at 488 nm. The cytoskeletons with FITC phalloidin (EX 405 nm, EM 500–540 nm) were green, and the autofluorescent DOX (EX 488 nm, EM 570–610 nm) was red. As shown in Fig. 2c, the fluorescence intensity of MCF-7 cells treated with AP-BWM-DOX and AP&SP-BWM-DOX was much higher than BWM-DOX. This result indicates that more AP-BWM-DOX and AP&SP-BWM-DOX were internalized into MCF-7 cells than BWM-DOX, which is consistent with flow cytometry, and again demonstrated the excellent targeting of AP&SP-BWM-DOX in MCF-7 cells.

3.3. *In vitro drug release and cytotoxicity of AP&SP-BWM-DOX*

In vitro cumulative release of DOX from BWM-DOX, AP-BWM-DOX, and AP&SP-BWM-DOX was tested in PBS with two different pH values (5.0 or 7.4) [57,58] at 37 °C. At pH 5.0, the DOX release profile was similar for all tested groups, and the maximum release was about 50% at 72 h (Fig. 3a–c). However, the DOX release from BWM-DOX was much faster than AP-BWM-DOX and AP&SP-BWM-DOX at pH 7.4. The maximum release of DOX from BWM-DOX was about 49.8% at 72 h, but that of AP-BWM-DOX and AP&SP-BWM-DOX was only about 21.1%. In addition, the DOX release from AP&SP-BWM-DOX has also been tested in PBS with 10% FBS at pH 7.4, and the maximum release of DOX was only about 25% at 72 h, indicating a low release rate of AP&SP-BWM-DOX in a simulated blood environment (Fig. S5). This result suggests that the AP ligand with pH-sensitive property avoids DOX release from the micelles during systemic circulation, but promotes drug release in the acidic tumor microenvironment or tumor cells. Compared to classic pH-sensitive micelles [57], AP modified micelles in this work show pH-protective drug release, with decreased drug release at pH = 7.4, but similar release levels compared to non-modified micelles at pH = 5.0, and additional SP modification does not influence this function. To reveal the mechanism of this interesting finding, biological material small-angle X-ray scattering (BioSAXS) was used to detect the peptide structure in different pH conditions (pH = 5.0 or 7.4) (Fig. S6) [59]. The Rg of AP is 102.4 Å for pH = 7.4, while it is 30.4 Å for pH = 5.0 (the theoretical simulation length is

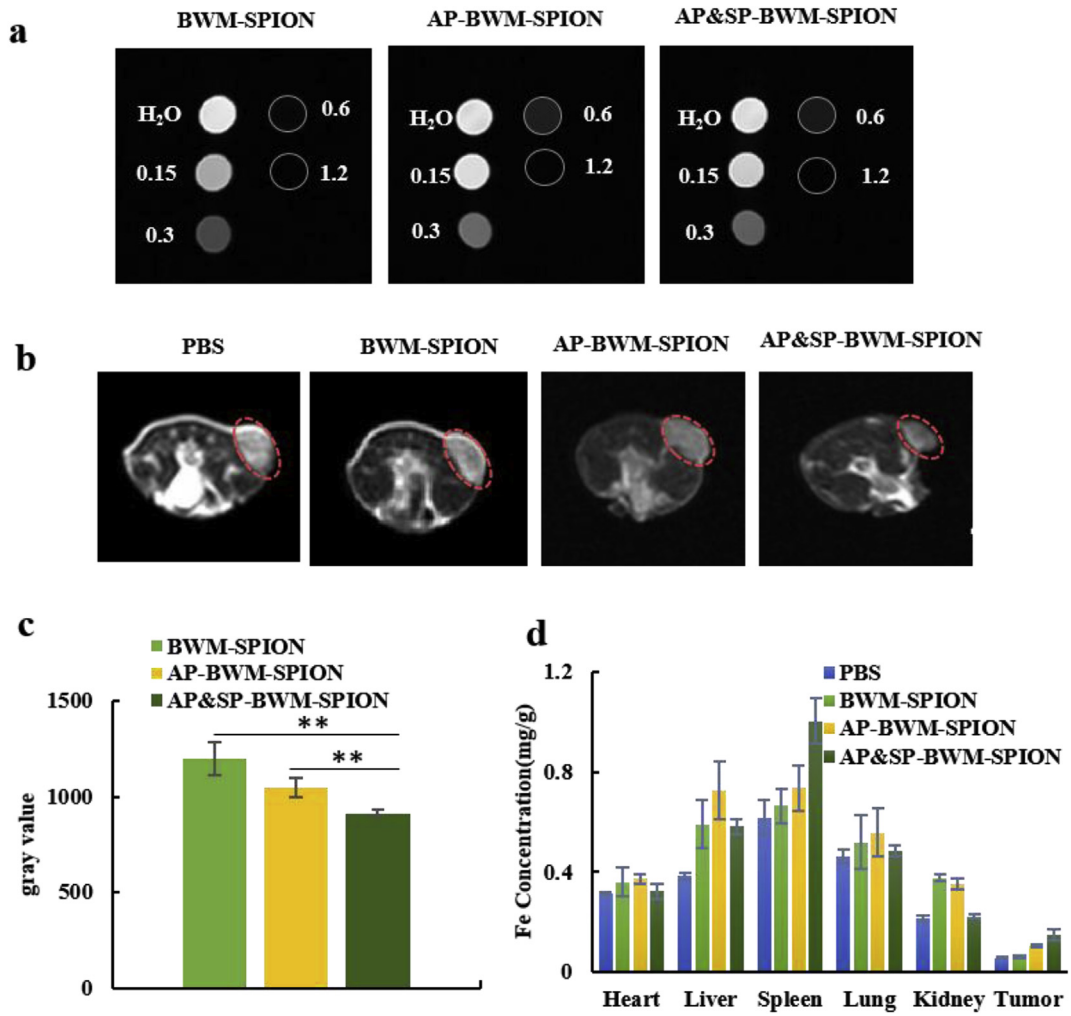

Fig. 4. *In vitro* and *in vivo* T_2-weighted MR imaging of AP&SP-BWM-SPION. a) *In vitro* T_2-weighted MR images of AP&SP-BWM-SPION at 0.15, 0.3, 0.6, and 1.2 mM Fe concentration (TR = 2000 ms, TE = 60 ms). b) *In vivo* T_2-weighted MR images of MCF-7 tumor bearing nude mice 20 h after i.v. injection of AP&SP-BWM-SPION (15 mg/kg for Fe). c) Gray value analysis of tumor area at 20 h. Mean ± SD ($n = 3$), **P < 0.01. d) Quantitative distribution analysis of Fe content in tumor, liver, spleen, lung, and kidney at 24 h after i.v. injection.

31.7 Å), suggesting AP might form a tetramer in physiological conditions and depolymerize in the acidic tumor microenvironment. Therefore, peptide structure changes in response to pH might be the main reason for this effect [60,61].

Further, the inhibition effect of AP&SP-BWM-DOX on MCF-7 cell growth was evaluated by MTT assay. The MCF-7 cells were incubated with free DOX, BWM-DOX, AP-BWM-DOX, and AP&SP-BWM-DOX for 24 h, and the DOX concentration was varied from 0.3 to 80 μg/mL. The effect of different proportions of BPLP-WPU to AP-BPLP-WPU (*w/w*) on the inhibition of MCF-7 cell growth were investigated (Fig. S7). The proportion of 25:1 (BPLP-WPU:AP-BPLP-WPU, *w/w*) produced the highest inhibition rate and lowest IC_{50} value, and was used for the following experiments. As shown in Fig. 3d, both AP-BWM-DOX and AP&SP-BWM-DOX showed significant inhibition on cell growth compared to free DOX and BWM-DOX for all tested concentrations. Further, the IC_{50} values were calculated for comparison (Fig. 3e), and the values of AP-BWM-DOX (1.68) and AP&SP-BWM-DOX (1.97) were significantly lower than free DOX (6.08) and BWM-DOX (9.79). This result shows that AP modification enhances cell inhibition, and SP modification doesn't obviously alter this effect. In addition, the inhibition effect of the micelles without DOX loading has also been envaluted. The inhibition rate of BWM and AP&SP-BWM was below 18.5% for all tested concentrations, indicating good biocompatibility of the prepared micelles (Fig. S8).

3.4. *In vitro and in vivo MRI of AP&SP-BWM-SPION*

In vitro MR performance of AP&SP-BWM-SPION was tested with a 0.47 T Micro MR instrument at a frequency of 23.3 MHz. The AP&SP-BWM-SPION demonstrated excellent T_2-MRI performance with an r_2 value of 319.76 mM^{-1} s^{-1}, and the ratio of r_2 to r_1 was about 7.37 (Fig. S9 and Table S3). Fig. 4a shows the T_2-weighted MR images of AP&SP-BWM-SPION at different concentrations. It could be seen that the T_2-weighted MR images became darker with increasing Fe concentration, which suggests that the AP&SP-BWM-SPION could be used as a potential T_2-MRI contrast agent.

In vivo T_2-MRI performance of AP&SP-BWM-SPION was investigated by a 1.5 T human clinical MR scanner. Fig. 4b shows the T_2-weighted MR images of MCF-7 tumor-bearing mice 20 h after intravenous (i.v.) injection. The AP&SP-BWM-SPION displayed a much darker signal than the other two groups, indicating more accumulation of SPION in the tumor sites. Further, the gray value of the tumor area was analyzed, and the value of AP&SP-BWM-SPION was significantly lower than the other two groups (Fig. 4c), suggesting that AP&SP-BWM-SPION has an excellent T_2-MR

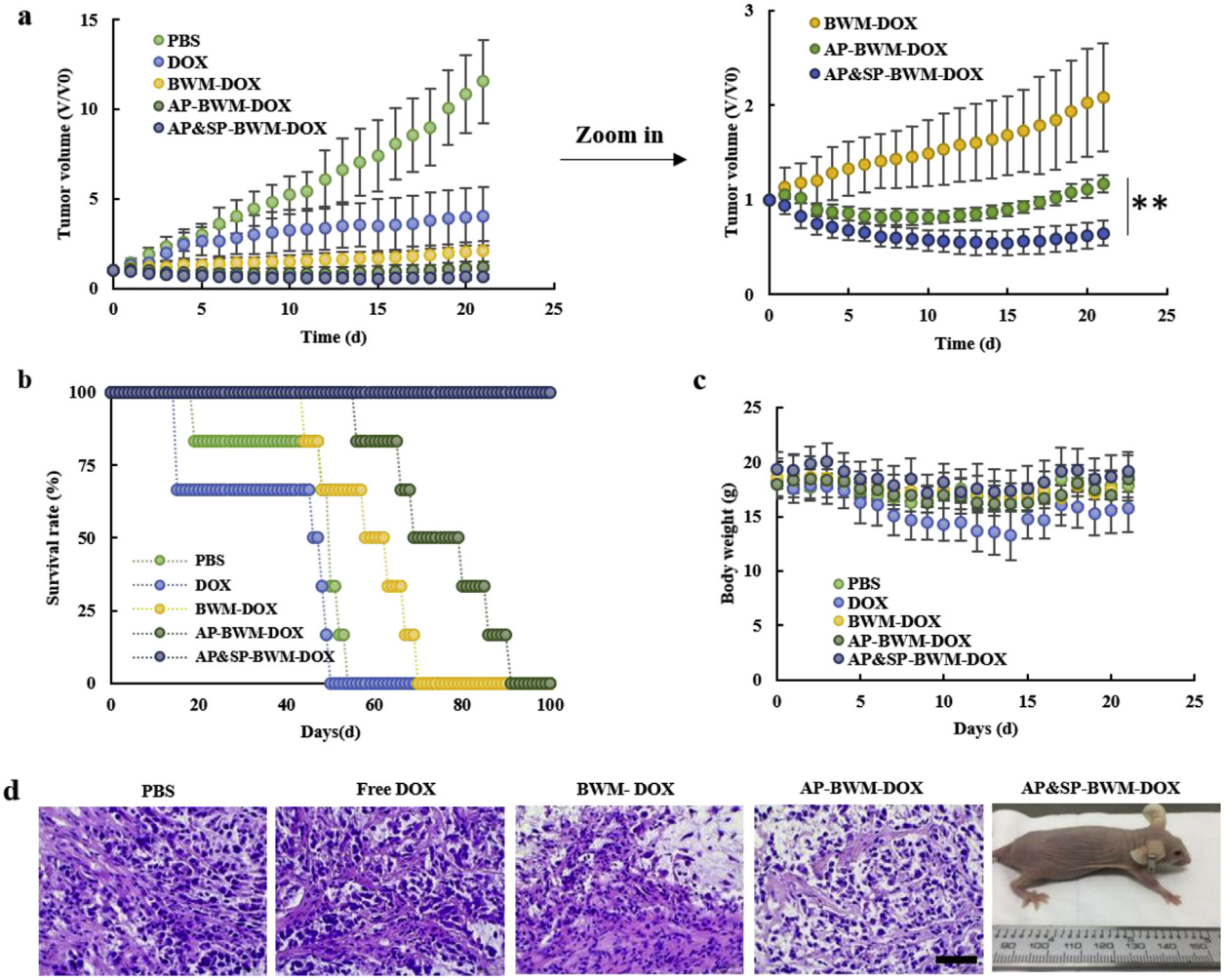

Fig. 5. *In vivo* antitumor studies of AP&SP-BWM-DOX in MCF-7 bearing nude mice. a) Relative tumor volume change after i.v. treatment with PBS, free DOX, BWM-DOX, AP-BWM-DOX, and AP&SP-BWM-DOX. (DOX = 5 mg/kg) b) Survival rate and c) body weight of mice after i.v. injection of different samples. Mean ± SD ($n = 6$), $^{**}P < 0.01$. d) H&E staining of tumors after 100 days of treatment. There was no tumor found in the group of AP&SP-BWM-DOX.

performance in MCF-7 tumor bearing mice.

To estimate the *in vivo* bio-distribution of AP&SP-BWM-SPION, tumors and main organs were harvested and nitrated with concentrated aqua regia after 24 h i.v. injection (Fig. 4d). The Fe ion amount in different organs was analyzed by ICP-OES. For AP&SP-BWM-SPION, the Fe ion amount in the tumor was much higher than BWM-SPION and AP-BWM-SPION, but Fe content in the liver, lung, and kidney was much lower than BWM-SPION and AP-BWM-SPION. As part of the mononuclear phagocyte system, macrophages mostly present in the liver, spleen, and kidney and are responsible for the clearance of foreign matter from the body [24–26]. The decreased accumulation in these organs suggests that the SP modification could minimize the opsonization of macrophages to nanoparticles. It is noteworthy that the Fe ion amount in the tumor of AP&SP-BWM-SPION treated group was two times higher than that of AP-BWM-DOX group. This might be attributed to the minimized clearance from liver and kidney during systemic circulation [62], leading to increased retention of SPION in the tumor sites. In general, these results suggest that the AP and SP modification collectively promoted the SPION accumulation in tumors, resulting in the improved MR signal.

3.5. In vivo antitumor efficacy

In vivo therapeutic efficacy evaluation of AP&SP-BWM-DOX was performed on a MCF-7 subcutaneous nude mouse model. The MCF-7 tumor bearing mice were intravenously injected with PBS, free DOX, BWM-DOX, AP-BWM-DOX, and AP&SP-BWM-DOX at a dose of 5 mg/kg DOX every other day six times. As shown in Fig. 5a, all tested groups showed tumor growth suppression compared to the PBS group. The relative tumor volume of AP-BWM-DOX and AP&SP-BWM-DOX groups was much smaller than BWM-DOX 11 days after i.v. injection, which could be attributed to the active targeting accumulation and pH responsive DOX release from the AP modified micelles in tumor sites. After 12 days, the relative tumor volume of AP-BWM-DOX group quickly became large, but that of the AP&SP-BWM-DOX group didn't show significant increase. This result suggests that AP&SP-BWM-DOX obtained the best inhibition effect on tumor growth. The tumor size difference between these groups was also observed by photographs of mice at 0, 7, and 14 days (Fig. S10). During the whole treatment, the body weight of mice was monitored. Compared with the fast decrease of body weight in free DOX group, there was no obvious change found in the other three groups with increased observation time (Fig. 5c). This might be due to the off-target induced severe side effects of DOX, which were effectively reduced by BWM-DOX, AP-BWM-DOX, and AP&SP-BWM-DOX. As shown in Fig. 6, numerous necrotic areas were observed on mice treated with DOX, who also showed serious side effects to vital organs and rapid body weight decline [63].

Survival time and percentage of the mice was observed for 100 days (Fig. 5b). There were different proportions of death of mice in PBS, free DOX, BWM-DOX, and AP-BWM-DOX groups, but there was a 100% survival rate of AP&SP-BWM-DOX after 100 days. After the experiment, tumor tissues were further evaluated by H&E staining (Fig. 5d). Compared to the PBS group, AP-BWM-DOX induced much more vacuolar chromatin, while the DOX group only increased the nuclear ratio which indicates that no obvious cell necrosis took place. Notably, no tumor could be found in the AP&SP-BWM-DOX

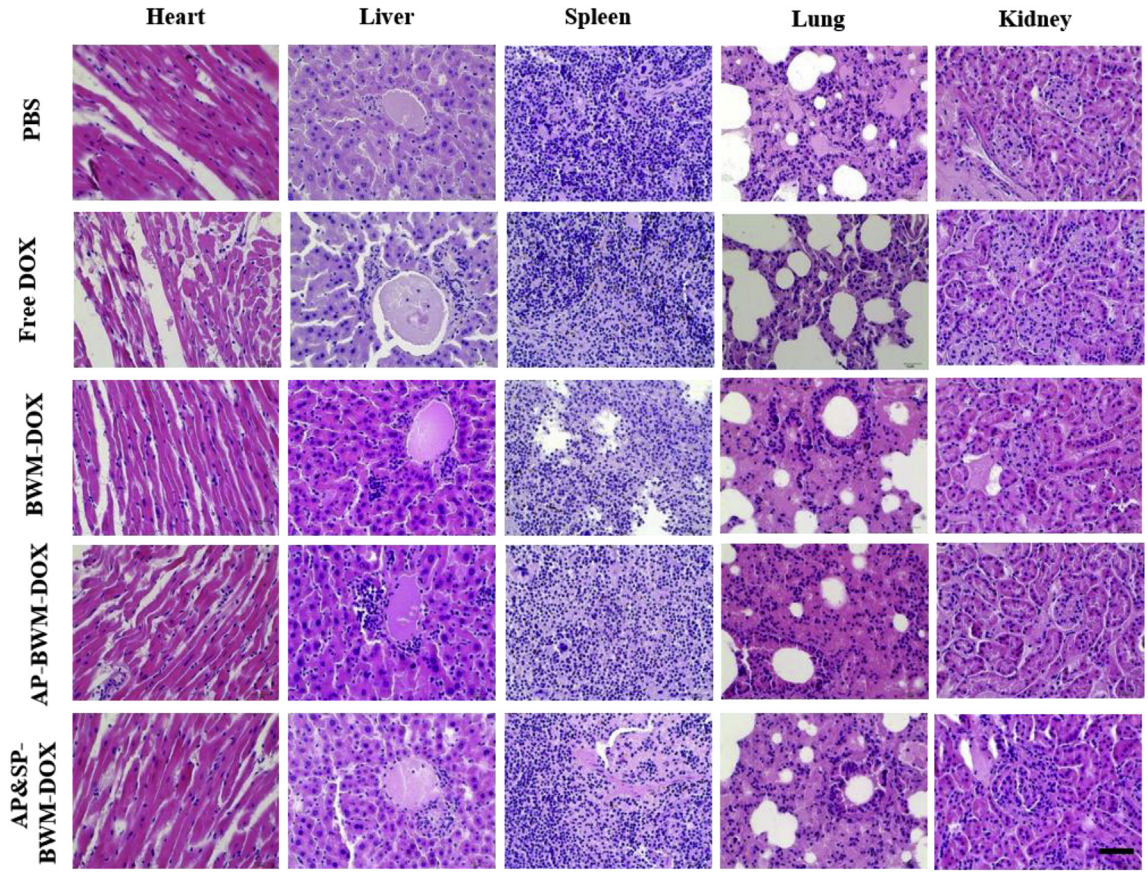

Fig. 6. H&E staining of vital organs of MCF-7 bearing nude mice after i.v. injection of PBS, free DOX, BWM-DOX, AP-BWM-DOX, and AP&SP-BWM-DOX. (DOX = 5 mg/kg) (Scale bar = 20 μm).

group (Fig. 5d). In addition, there was no obvious abnormality in other vital organs (i.e., heart, liver, spleen, lung, and kidney), indicating the AP&SP-BWM-DOX attained significant biosafety (Fig. 6). Homological analysis also showed no significant changes between PBS and tested groups (Fig. S11). Taken together, these results demonstrated that AP and SP collectively enhanced drug retention in the tumor, improved anticancer therapeutic efficacy, and reduced side effects to vital organs.

3.6. Pharmacokinetics study

The pharmacokinetics of DOX were further investigated in order to evaluate the pharmacological effect of the AP&SP-BWM-DOX *in vivo* (Fig. S12). As expected, AP&SP-BWM-DOX showed a prolong elimination half-life ($t_{1/2}$) in the blood circulation compared with the free DOX, which was 7.8 and 1.9 h, respectively. The C_{max} of AP&SP-BWM-DOX (54.8 μg/mL) in the plasma was 4.8-fold of free DOX (11.3 μg/mL). In addition, the area-under-the-curve ($AUC_{0\text{-}24h}$) of AP&SP-BWM-DOX (199.3 μg/mL*h) was 20-fold than free DOX (10.0 μg/mL*h). The data indicated that AP&SP-BWM-DOX significantly ameliorated the pharmacokinetic parameters of DOX *in vivo* by prolonging the blood circulation half-life and more likely to preferentially accumulate in tumors than free DOX by retarding the blood clearance of the drug.

In addition, the pharmacokinetics of Fe has also been investigated to understand the effect of AP&SP-BWM-SPION *in vivo* (Fig. S13). The $t_{1/2}$ of AP&SP-BWM-SPION (69.3 h) was 12.7-fold than that of SPION (5.4 h), indicating a longer circulation time for AP&SP-BWM-SPION in the blood. The C_{max} of AP&SP-BWM-SPION and SPION was about 742.9 and 656.7 μg/mL, respectively. Further, the $AUC_{0\text{-}24h}$ of AP&SP-BWM-SPION (6519.9 μg/mL*h) was 2.5-fold than of SPION (2626.8 μg/mL*h). Taken together, our data suggests that AP and SP modified micelles can also improve the blood circulation of SPION *in vivo*, providing more chance for SPION accumulation in tumor sites.

4. Conclusion

In this study, Y_1R ligand AP and antiphagocytosis SP functionalized novel BPLP-WPU micelles were first reported to avoid premature drug leakage and macrophage opsonization during micelle storage and systemic circulation. AP modification not only improved micelle targeting to the tumor cells, but also promoted drug release under the acidic tumor microenvironment. The AP and SP combination not only reduced the accumulation of micelles in liver and kidney, but also enhanced the specific targeting and high retention of SPION or DOX loaded micelles in tumor sites, generating excellent MR signal and therapeutic efficacy with prolonged survival time *in vivo*. This study may pave the way for more accurate and safer Y_1R overexpressed breast cancer diagnosis and treatment.

Acknowledgements

This work was supported by Youth Innovation Promotion Association Foundation, CAS (2017340 to Juan Li), Science Technology Department of Zhejiang Province (2016C33093 to Juan Li), Natural Science Foundation of China (Grant No. 51303196 to Juan Li, U1432114 to Aiguo Wu), Special Program for Applied Research on Super Computation of the NSFC-Guangdong Joint Fund (the second phase) (U1501501 to Juan Li and Aiguo Wu), the Science & Technology Bureau of Ningbo City (2015C50004, 2015B11002, and 2017C110022), Zhejiang Province Financial Supporting (2017C03042, LY18H180011), and CAS Interdiscipline Innovation Team. We acknowledge Miss. Siqi Wang and Dr. Jianhua Wang from Ningbo University Hospital for their help in hematological analysis. We thank Miss. Ruifen Zou for her help in animal experiments and Mr. Xuzhe Zhang from Beijing Dryas Pharma-Tech Co., Ltd. for his help of in data analysis of pharmacokenetics. Furthermore, the authors also acknowledge Shanghai Synchrotron Radiation Facility at Line BL15U (No. h15sr0021) used for X-ray fluorescence imaging and BL19U2 used for small-angle X-ray scattering, and National Synchrotron Radiation Laboratory in Hefei used for soft X-ray imaging (No. 2016-HLS-PT-002193).

Appendix A. Supplementary data

Supplementary data related to this article can be found at https://doi.org/10.1016/j.biomaterials.2018.04.002.

References

[1] C.E. DeSantis, J. Ma, A.N. Sauer, L.A. Newman, A. Jemal, Breast cancer statistics, 2017, racial disparity in mortality by state, CA Canc. J. Clin. 67 (2017) 439–448.
[2] L.A. Torre, F. Bray, R.L. Siegel, J. Ferlay, J. Lortet-Tieulent, A. Jemal, Global cancer statistics, 2012, CA Canc. J. Clin. 65 (2015) 87–108.
[3] F. Mottaghitalab, M. Farokhi, M.A. Shokrgozar, F. Atyabi, H. Hosseinkhani, Silk fibroin nanoparticle as a novel drug delivery system, J. Contr. Release 206 (2015) 161–176.
[4] M. Mohammad-Taheri, E. Vasheghani-Farahani, H. Hosseinkhani, S.A. Shojaosadati, M. Soleimani, Fabrication and characterization of a new MRI contrast agent based on a magnetic dextran-spermine nanoparticle system, Iran Polym. J. 21 (2012) 239–251.
[5] M. Langer, F. Kratz, B. Rothen-Rutishauser, H. Wunderli-Allenspach, A.G. Beck-Sicklinger, Novel peptide conjugates for tumor-specific chemotherapy, J. Med. Chem. 44 (2001) 1341–1348.
[6] M. Mahmoudi, K. Azadmanesh, M.A. Shokrgozar, W.S. Journeay, S. Laurent, Effect of nanoparticles on the cell life cycle, Chem. Rev. 111 (2011) 3407–3432.
[7] J. Shi, P.W. Kantoff, R. Wooster, O.C. Farokhzad, Cancer nanomedicine: progress, challenges and opportunities, Nat. Rev. Canc. 17 (2017) 20–37.
[8] N. Bertrand, J. Wu, X. Xu, N. Kamaly, O.C. Farokhzad, Cancer nanotechnology: the impact of passive and active targeting in the era of modern cancer biology, Adv. Drug Deliv. Rev. 66 (2014) 2–25.
[9] H. Hosseinkhani, M. Hosseinkhani, Y. Chen, K. Subramani, A.J. Domb, Innovative technology of engineering magnetic DNA nanoparticles for gene therapy, Int. J. Nanotechnol. 8 (2011) 724–734.
[10] M. Ghadiri, E. Vasheghani-Farahani, F. Atyabi, F. Kobarfard, H. Hosseinkhani, *In vitro* assessment of magnetic dextran-spermine nanoparticles for capecitabine delivery to cancerous cells, Iran J. Pharm. Res. 16 (2017) 1320–1334.
[11] W. He, H. Hosseinkhani, R. Mohammadinejad, Z. Roveimiab, D. Hueng, K. Ou, A.J. Domb, Polymeric nanoparticles for therapy and imaging, Polym. Adv. Technol. 25 (2014) 1216–1225.
[12] X.D. Xu, P.E. Saw, W. Tao, Y.J. Li, X.Y. Ji, S. Bhasin, Y.L. Liu, D. Ayyash, J. Rasmussen, M. Huo, J.J. Shi, O.C. Farokhzad, ROS-responsive polyprodrug nanoparticles for triggered drug delivery and effective cancer therapy, Adv. Mater. 29 (2017) 1700141.
[13] E. Nance, C. Zhang, T.Y. Shih, Q. Xu, B.S. Schuster, J. Hanes, Brain-penetrating nanoparticles improve paclitaxel efficacy in malignant glioma following local administration, ACS Nano 8 (2014) 10655–10664.
[14] Z. Xie, Y. Zhang, L. Liu, H. Weng, R.P. Mason, L. Tang, K.T. Nguyen, J.-T. Hsieh, J. Yang, Development of intrinsically photoluminescent and photostable polylactones, Adv. Mater. 26 (2014) 4491–4496.
[15] J. Hu, J. Guo, Z. Xie, D. Shan, E. Gerhard, G. Qian, J. Yang, Fluorescence imaging enabled poly(lactide-co-glycolide), Acta Biomater. 29 (2016) 307–319.
[16] M. Korner, J.C. Reubi, NPY receptors in human cancer: a review of current knowledge, Peptides 28 (2007) 419–425.
[17] J.C. Reubi, M. Gugger, B. Waser, J.C. Schaer, Y_1-mediated effect of neuropeptide Y in cancer: breast carcinomas as targets, Canc. Res. 61 (2001) 4636–4641.
[18] J. Li, Y. Tian, A. Wu, Neuropeptide Y receptors: a promising target for cancer imaging and therapy, Regener. Biomater. 2 (2015) 215–219.
[19] I.U. Khan, D. Zwanziger, I. Böhme, M. Javed, H. Naseer, S.W. Hyder, A.G. Beck-Sickinger, Breast-cancer diagnosis by neuropeptide Y analogues: from synthesis to clinical application, Angew. Chem. Int. Ed. 49 (2010) 1155–1158.
[20] S. Hofmann, S. Maschauer, T. Kuwert, A.G. Beck-Sickinger, O. Prante, Synthesis and in vitro and in vivo evaluation of an (18)F-labeled neuropeptide Y analogue for imaging of breast cancer by PET, Mol. Pharm. 12 (2015) 1121–1130.
[21] B. Guerin, V. Dumulon-Perreault, M.C. Tremblay, S. Ait-Mohand, P. Fournier, C. Dubuc, S. Authier, F. Benard, [Lys(DOTA)$_4$]BVD15, a novel and potent neuropeptide Y analog designed for Y1 receptor-targeted breast tumor imaging, Bioorg. Med. Chem. Lett 20 (2010) 950–953.
[22] J. Li, Z.Y. Shen, X.H. Ma, W.Z. Ren, L.C. Xiang, A. Gong, T. Xia, J.M. Guo, A.G. Wu,

Neuropeptide Y Y-1 receptors meditate targeted delivery of anticancer drug with encapsulated nanoparticles to breast cancer cells with high selectivity and its potential for breast cancer therapy, ACS Appl. Mater. Interfaces 7 (2015) 5574–5582.
[23] J. Li, Y. Tian, D. Shan, A. Gong, L. Zeng, W. Ren, L. Xiang, E. Gerhard, J. Zhao, J. Yang, A. Wu, Neuropeptide Y Y_1 receptor-mediated biodegradable photoluminescent nanobubbles as ultrasound contrast agents for targeted breast cancer imaging, Biomaterials 116 (2017) 106–117.
[24] Q. Sun, Z. Zhou, N. Qiu, Y. Shen, Rational design of cancer nanomedicine: nanoproperty integration and synchronization, Adv. Mater. 29 (2017) 1606628–1606634.
[25] R. Yang, T. Wei, H. Goldberg, W. Wang, K. Cullion, D.S. Kohane, Getting drugs across biological barriers, Adv. Mater. 29 (2017) 1606596–1606602.
[26] R.S. Flannagan, V. Jaumouille, S. Grinstein, The cell biology of phagocytosis, Annu. Rev. Pathol. 7 (2012) 61–98.
[27] S. Wilhelm, A.J. Tavares, Q. Dai, S. Ohta, J. Audet, H.F. Dvorak, W.C.W. Chan, Analysis of nanoparticle delivery to tumours, Nat. Rev. Mater. 1 (2016) 16014.
[28] M.A. Miller, S. Gadde, C. Pfirschke, C. Engblom, M.M. Sprachman, R.H. Kohler, K.S. Yang, A.M. Laughney, G. Wojtkiewicz, N. Kamaly, S. Bhonagiri, M.J. Pittet, O.C. Farokhzad, R. Weissleder, Predicting therapeutic nanomedicine efficacy using a companion magnetic resonance imaging nanoparticle, Sci. Transl. Med. 7 (2015), 314ra183.
[29] H. Choi, T. Liu, K. Nath, R. Zhou, I.W. Chen, Peptide nanoparticle with pH-sensing cargo solubility enhances cancer drug efficiency, Nano Today 13 (2017) 15–22.
[30] T. Lammers, F. Kiessling, M. Ashford, W. Hennink, D. Crommelin, G. Storm, Cancer nanomedicine: is targeting our target? Nat. Rev. Mater. 1 (2016) 16069.
[31] P.L. Rodriguez, T. Harada, D.A. Christian, D.A. Pantano, R.K. Tsai, D.E. Discher, Minimal "Self" peptides that inhibit phagocytic clearance and enhance delivery of nanoparticles, Science 339 (2013) 971–975.
[32] P.A. Oldenborg, A. Zheleznyak, Y.F. Fang, C.F. Lagenaur, H.D. Gresham, F.P. Lindberg, Role of CD47 as a marker of self on red blood cells, Science 288 (2000) 2051–2057.
[33] E.J. Brown, W.A. Frazier, Integrin-associated protein (CD47) and its ligands, Trends Cell Biol. 11 (2001) 130–135.
[34] R.A. Cardone, V. Casavola, S.J. Reshkin, The role of disturbed pH dynamics and the Na+/H+ exchanger in metastasis, Nat. Rev. Canc. 5 (2005) 786–795.
[35] L.I. Cardenas-Navia, R.A. Richardson, M.W. Dewhirst, Targeting the molecular effects of a hypoxic tumor microenvironment, Front. Biosci. 12 (2007) 4061–4078.
[36] G. Baronzio, L. Schwartz, M. Kiselevsky, A. Guais, E. Sanders, G. Milanesi, M. Baronzio, I. Freitas, Tumor interstitial fluid as modulator of cancer inflammation, thrombosis, immunity and angiogenesis, Anticanc. Res. 32 (2012) 405–414.
[37] T.J. Ji, Y. Zhao, Y.P. Ding, G.J. Nie, Using functional nanomaterials to target and regulate the tumor microenvironment: diagnostic and therapeutic applications, Adv. Mater. 25 (2013) 3508–3525.
[38] S. Romero-Garcia, J.S. Lopez-Gonzalez, J.L. Baez-Viveros, D. Aguilar-Cazares, H. Prado-Garcia, Tumor cell metabolism an integral view, Canc. Biol. Ther. 12 (2011) 939–948.
[39] J. Liu, Y. Huang, A. Kumar, A. Tan, S. Jin, A. Mozhi, X.-J. Liang, pH-sensitive nano-systems for drug delivery in cancer therapy, Biotechnol. Adv. 32 (2014) 693–710.
[40] L. Shen, Y. Huang, D. Chen, F. Qiu, C. Ma, X. Jin, X. Zhu, G. Zhou, Z. Zhang, pH-responsive aerobic nanoparticles for effective photodynamic therapy, Theranostics 7 (2017) 4537–4550.
[41] B. Chen, W. Dai, B. He, H. Zhang, X. Wang, Y. Wang, Q. Zhang, Current multistage drug delivery systems based on the tumor microenvironment, Theranostics 7 (2017) 538–558.
[42] B.X. Zhao, Y. Zhao, Y. Huang, L.M. Luo, P. Song, X. Wang, S. Chen, K.F. Yu, X. Zhang, Q. Zhang, The efficiency of tumor-specific pH-responsive peptide-modified polymeric micelles containing paclitaxel, Biomaterials 33 (2012) 2508–2520.
[43] M.J. Turk, J.A. Reddy, J.A. Chmielewski, P.S. Low, Characterization of a novel pH-sensitive peptide that enhances drug release from folate-targeted liposomes at endosomal pHs, Bba-Biomembranes 1559 (2002) 56–68.
[44] Z. Li, L.P. Qiu, Q. Chen, T.N. Hao, M.X. Qiao, H.X. Zhao, J. Zhang, H.Y. Hu, X.L. Zhao, D.W. Chen, L. Mei, pH-sensitive nanoparticles of poly(L-histidine)-poly(lactide-co-glycolide)-tocopheryl polyethylene glycol succinate for anti-tumor drug delivery, Acta Biomater. 11 (2015) 137–150.
[45] X. Li, M. Fu, J. Wu, C.Y. Zhang, X. Deng, A. Dhinakar, W.L. Huang, H. Qian, L. Ge, pH-sensitive peptide hydrogel for glucose-responsive insulin delivery, Acta Biomater. 51 (2017) 294–303.
[46] H. Wu, L. Zhu, V.P. Torchilin, pH-sensitive poly(histidine)-PEG/DSPE-PEG co-polymer micelles for cytosolic drug delivery, Biomaterials 34 (2013) 1213–1222.
[47] Y. Zhao, W. Ren, T. Zhong, S. Zhang, D. Huang, Y. Guo, X. Yao, C. Wang, W.Q. Zhang, X. Zhang, Q. Zhang, Tumor-specific pH-responsive peptide-modified pH-sensitive liposomes containing doxorubicin for enhancing glioma targeting and anti-tumor activity, J. Contr. Release 222 (2016) 56–66.
[48] R.M. Soll, M.C. Dinger, I. Lundell, D. Larhammer, A.G. Beck-Sickinger, Novel analogues of neuropeptide Y with a preference for the Y1-receptor, Eur. J. Biochem. 268 (2001) 2828–2837.
[49] X.H. Ma, A. Gong, B. Chen, J.J. Zheng, T.X. Chen, Z.Y. Shen, A.G. Wu, Exploring a new SPION-based MRI contrast agent with excellent water-dispersibility, high specificity to cancer cells and strong MR imaging efficacy, Colloid Surf. B Biointerfaces 126 (2015) 44–49.
[50] E. Jin, B. Zhang, X. Sun, Z. Zhou, X. Ma, Q. Sun, J. Tang, Y. Shen, E. Van Kirk, W.J. Murdoch, M. Radosz, Acid-active cell-penetrating peptides for in vivo tumor-targeted drug delivery, J. Am. Chem. Soc. 135 (2013) 933–940.
[51] M.Y. Hu, J.F. Zhu, L.Y. Qiu, Polymer micelle-based combination therapy of paclitaxel and resveratrol with enhanced and selective antitumor activity, RSC Adv. 4 (2014) 64151–64161.
[52] W.Z. Ren, Y. Yan, L.Y. Zeng, Z.Z. Shi, A. Gong, P. Schaaf, D. Wang, J.S. Zhao, B.B. Zou, H.S. Yu, G. Chen, E.M.B. Brown, A.G. Wu, A near infrared light triggered hydrogenated black TiO_2 for cancer photothermal therapy, Adv. Healthc. Mater. 4 (2015) 1526–1536.
[53] E. Frohlich, The role of surface charge in cellular uptake and cytotoxicity of medical nanoparticles, Int. J. Nanomed. 7 (2012) 5577–5591.
[54] S. Behzadi, V. Serpooshan, W. Tao, M.A. Hamaly, M.Y. Alkawareek, E.C. Dreaden, D. Brown, A.M. Alkilany, O.C. Farokhzad, M. Mahmoudi, Cellular uptake of nanoparticles: journey inside the cell, Chem. Soc. Rev. 46 (2017) 4218–4244.
[55] W. Ren, M.Z. Iqbal, L. Zeng, T. Chen, Y. Pan, J. Zhao, H. Yin, L. Zhang, J. Zhang, A. Li, A. Wu, Black TiO_2 based core-shell nanocomposites as doxorubicin carriers for thermal imaging guided synergistic therapy of breast cancer, Nanoscale 9 (2017) 11195–11204.
[56] L. Zeng, Y. Pan, R. Zou, J. Zhang, Y. Tian, Z. Teng, S. Wang, W. Ren, X. Xiao, J. Zhang, L. Zhang, A. Li, G. Lu, A. Wu, 808 nm-excited upconversion nanoprobes with low heating effect for targeted magnetic resonance imaging and high-efficacy photodynamic therapy in HER2-overexpressed breast cancer, Biomaterials 103 (2016) 116–127.
[57] R.P. Johnson, Y.-I. Jeong, E. Choi, C.-W. Chung, D.H. Kang, S.-O. Oh, H. Suh, I. Kim, Biocompatible poly(2-hydroxyethyl methacrylate)-b-poly(L-histidine) hybrid materials for pH-sensitive intracellular anticancer drug delivery, Adv. Funct. Mater. 22 (2012) 1058–1068.
[58] K.C. Barick, S. Singh, N.V. Jadhav, D. Bahadur, B.N. Pandey, P.A. Hassan, pH-responsive peptide mimic shell cross-linked magnetic nanocarriers for combination therapy, Adv. Funct. Mater. 22 (2012) 4975–4984.
[59] I.S. Dmitri, H.J.K. Michel, Small-angle scattering studies of biological macromolecules in solution, Rep. Prog. Phys. 66 (2003) 1735–1782.
[60] C. Kinnear, T.L. Moore, L. Rodriguez-Lorenzo, B. Rothen-Rutishauser, A. Petri-Fink, Form follows function: nanoparticle shape and its implications for nanomedicine, Chem. Rev. 117 (2017) 11476–11521.
[61] O.A. Andreev, A.D. Dupuy, M. Segala, S. Sandugu, D.A. Serra, C.O. Chichester, D.M. Engelman, Y.K. Reshetnyak, Mechanism and uses of a membrane peptide that targets tumors and other acidic tissues in vivo, Proc. Natl. Acad. Sci. U. S. A 104 (2007) 7893–7898.
[62] Z. Gao, Y. Hou, J. Zeng, L. Chen, C. Liu, W. Yang, M. Gao, Tumor microenvironment-triggered aggregation of antiphagocytosis ^{99m}Tc-labeled Fe_3O_4 nanoprobes for enhanced tumor imaging in vivo, Adv. Mater. 29 (2017) 1701095–1701101.
[63] X. Sun, R. Du, L. Zhang, G. Zhang, X. Zheng, J. Qian, X. Tian, J. Zhou, J. He, Y. Wang, Y. Wu, K. Zhong, D. Cai, D. Zou, Z. Wu, A pH-responsive yolk-like nanoplatform for tumor targeted dual-mode magnetic resonance imaging and chemotherapy, ACS Nano 11 (2017) 7049–7059.